REPORT DOCUMENTATION PAGE

AFRL-SR-AR-TR-08-0540

1. REPORT DATE *(DD-MM-YYYY)*	2. REPORT TYPE	3. DATES COVERED *(From - To)*
9/30/2008	Final Performance Report	07/01/2005 - 06/30/2008

4. TITLE AND SUBTITLE
"New Widely Tunable, Room-Temperature Terahertz Coherent Sources"

5a. CONTRACT NUMBER

5b. GRANT NUMBER
FA9550-05-1-0435

5c. PROGRAM ELEMENT NUMBER

6. AUTHOR(S)
Federico Capasso

5d. PROJECT NUMBER

5e. TASK NUMBER

5f. WORK UNIT NUMBER

7. PERFORMING ORGANIZATION NAME(S) AND ADDRESS(ES)

President and Fellows of Harvard College — Office for Sponsored Research, Holyoke Center, Suite 600, 1350 Massachusetts Ave., Cambridge, MA 02138

8. PERFORMING ORGANIZATION REPORT NUMBER

9. SPONSORING / MONITORING AGENCY NAME(S) AND ADDRESS(ES)
Air Force Office of Scientific Research
875 N Randolph St
Arlington VA 22203

10. SPONSOR/MONITOR'S ACRONYM(S)
AFOSR

11. SPONSOR/MONITOR'S REPORT NUMBER(S)

12. DISTRIBUTION / AVAILABILITY STATEMENT
Distribution A: Approved for Public Release

13. SUPPLEMENTARY NOTES

14. ABSTRACT The objective of this proposal was to develop a new type of THz semiconductor sources that are injection-pumped, efficient, compact, narrowband, tunable, and can operate at room temperature. The proposed device was a mid-infrared InGaAs/AlInAs Quantum Cascade Laser (QCLs) with the waveguide core containing a multi-functional coupled-quantum-well active region that supports both laser action in the mid-infrared and THz generation due to resonant coherent beating of two laser modes. During the course of the work a path was also found to substantially improve the temperature performance and directionality of conventional THz QCLs in which an electronic transition is used for the direct generation of THz radiation. The following was accomplished: first room temperature operation of an lectrically pumped quantum cascade laser based THz source, using intra-cavity nonlinear optics; record operating temperature (180K) of a conventional THz Quantum Cascade Laser, using a copper double metal waveguide for low loss; surface emitting THz QCLs with low beam divergence.

15. SUBJECT TERMS

16. SECURITY CLASSIFICATION OF:			17. LIMITATION OF ABSTRACT	18. NUMBER OF PAGES	19a. NAME OF RESPONSIBLE PERSON
a. REPORT	b. ABSTRACT	c. THIS PAGE			19b. TELEPHONE NUMBER *(include area code)*

Final Performance Report to AFOSR

on AFOSR contract FA9550-05-1-0435

New widely tunable room-temperature Terahertz coherent sources

Reported period: July 1, 2005 – June 30, 2008

PI at HARVARD UNIVERSITY: Prof. Federico Capasso
School of Engineering and Applied Sciences
Harvard University
205A Pierce, 29 Oxford St.
Cambridge MA 02138
Tel. 617-3847611
Fax 617-495-2875
Email: capasso@seas.harvard.edu

Co-PI at TAMU: Prof. Alexey Belyanin
Department of Physics, Texas A&M University,
4242 TAMU, College Station, TX 77843-4242
Tel.: 979-845-7785
Fax: 979-845-2590
E-mail: belyanin@tamu.edu

1. Objectives

The objective of this proposal was to develop a new type of THz semiconductor sources that are injection-pumped, efficient, compact, narrowband, tunable, and can operate at room temperature. The proposed device was a mid-infrared InGaAs/AlInAs Quantum Cascade Laser (QCLs) with the waveguide core containing a multi-functional coupled-quantum-well active region that supports both laser action in the mid-infrared and THz generation due to resonant coherent beating of two laser modes.

2. Accomplishments

a. *First room temperature operation of an electrically pumped quantum cascade laser based THz source.* The THz radiation was generated by the coherent intracavity beating of two mid-ir QC lasers. THz QCLs have not yet operated at thermoelectric cooler temperature

b. *Record operating temperature (180K) of a THz QCLs.* This was achieved by the use of an improved metal-metal waveguide using copper instead of gold, which reduces the optical losses

c. *Surface emitting THz QCLs with low divergence.* This approach allows circumventing a major problem of THz QCls: the trapping of light by the subwavelength aperture associated with the double metal waveguide and the attendant reduce power output and increased divergence.

3. Electrically pumped QCL THz source based on difference frequency generation

The terahertz spectral range (λ=30-300μm) has long been devoid of compact electrically pumped room temperature semiconductor sources. Despite recent progress with terahertz quantum cascade lasers, existing devices still require cryogenic cooling. An alternative way to produce terahertz radiation is frequency down-conversion in a nonlinear optical crystal using infrared or visible pump lasers. This approach offers broad spectral tunability and does work at room temperature; however it requires powerful laser pumps and a more complicated optical setup, resulting in bulky and unwieldy sources. The focus of this project was to the demonstration of monolithically integrated device designed to combine the advantages of electrically pumped semiconductor lasers and nonlinear optical sources. The device is a dual-wavelength quantum cascade laser with the active region engineered to possess giant second-order nonlinear susceptibility associated with intersubband transitions in coupled quantum wells so as to produce THz radiation by difference-frequency generation (DFG). In its first implementation the source produced terahertz output at λ=60 μm at 10 with ~ 5 nW of power. Subsequently with improved design dramatic performance improvement was achieved: the device operated with 7 μW output power at 80 K, 1 μW output at 250K, and still approximately 300 nW output at 300 K.

Theory and quantum design

DFG is a nonlinear optical process in which two beams at frequencies ω_1 and ω_2 interact in a medium with second-order nonlinear susceptibility, $\chi^{(2)}$, to produce radiation at frequency $\omega=\omega_1-\omega_2$. The intensity of the wave at frequency $\omega=\omega_1-\omega_2$ is given by the expression

$$W(\omega=\omega_1-\omega_2)=\frac{\omega^2}{8\varepsilon_0 c^3 n(\omega_1)n(\omega_2)n(\omega)}\left|\chi^{(2)}\right|^2\times\frac{W(\omega_1)W(\omega_2)}{S_{eff}}\times l_{coh}^2, \qquad (1)$$

where $l_{coh}=1\Big/\left(\left|\vec{k}-(\vec{k}_1-\vec{k}_2)\right|^2+(\alpha/2)^2\right)$ is the coherence length, $W(\omega_i)$, $n(\omega_i)$, and $\vec{k}_i$ are the power, refractive index, and the wave vector of the beam at frequency ω_i, respectively, α stands for the losses at DFG frequency, S_{eff} is the effective area of interaction, and we assumed that the medium is transparent for both pumps and neglected the depletion of the pump powers in the DFG process. It follows from Eq. (1) that, for

efficient DFG, one needs to use materials with large $\chi^{(2)}$, input beams of high intensity, and achieve low losses and phase matching, $\left|\vec{k}-(\vec{k}_1-\vec{k}_2)\right|\approx 0$.

The problem of resonance of the pumps and of the DFG with specific transitions, required to achieve a large enhancement of the susceptibilities but which causes absorption thus drastically reducing the conversion efficiency, was solved by designing an *active* nonlinear semiconductor device with the coupled quantum wells states providing both laser gain and giant $\chi^{(2)}$. In this case, instead of resonant absorption of the pump frequency, one has laser gain, whereas intra-waveguide generation of all interacting fields provides their tightest possible confinement and overlap.

The devices are based on an $In_{0.53}Ga_{0.47}As/In_{0.52}Al_{0.48}As$ heterostructure grown by Molecular Beam Epitaxy (MBE), with upper InP waveguide cladding re-grown by Metalorganic Chemical Vapor Deposition (MOCVD). The MBE growth started on an InP substrate, n-doped to 9×10^{16} cm^{-3}, with 30 stages of the "double-phonon resonance" active region, designed to emit at 10.5 μm, followed by 100-nm-thick GaInAs spacer, n-doped to 3×10^{16} cm^{-3}, and 30 stages of the "bound-to-continuum" active region, designed to emit at 8.9 μm. The layer sequences for the two sections are listed in the captions to Fig. 1. The MBE growth ended with a 50-nm-thick GaInAs layer, n-doped to 3×10^{16} cm^{-3}. An upper waveguide cladding, consisting of 3.5-μm-thick and 0.2-μm-thick InP layers, n-doped to 5×10^{16} cm^{-3} and 5×10^{18} cm^{-3}, respectively, was then overgrown by MOCVD.
The bound-to-continuum section in our devices is expected to have the largest $\chi^{(2)}$ for DFG. The conduction band diagram of a single period of this section, along with the schematics of the THz DFG process, is shown in Fig. 1.

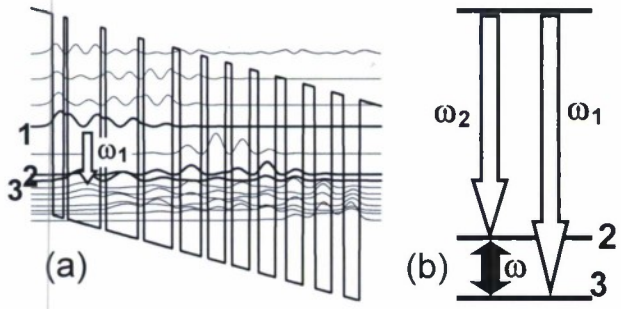

Fig. 1. (a) Calculated conduction-band diagram of one period of a 'bound-to-continuum' quantum-cascade-laser section at applied bias of 37 kV/cm. The wavy curves represent the moduli squared of the wavefunctions. The electron states important for DFG are shown in bold and labeled 1 to 3. The layer sequence (in nm), starting from the injection barrier, for this structure is **4.0**/2.4/**0.7**/6.5/**0.8**/6.4/**0.8**/5.8/**2.2**/4.0/**1.3**/3.8/**1.4**/3.7/**1.5**/3.6/**1.9**/3.6/**2.5**/3.6/**2.5**/3.5. (The layer sequence for one period of a "double-phonon resonance" section which generates frequency ω_2 is **4.0**/2.0/**0.7**/6.0/**0.9**/5.9/**1.0**/5.2/**1.4**/3.8/**1.2**/3.2/**1.2**/3.2/**1.6**/ 3.1/**1.9**/3.1/**2.2**/3.0/**2.2**/2.9.) The barriers are indicated in bold face and the underlined layers are doped to n=3×10^{17} cm^{-3}. (b) Diagram showing the DFG process between the electron states in the 'bound-to-continuum' section.

For a resonant DFG, the expression for the nonlinear susceptibility simplifies to:

$$\chi^{(2)}(\omega=\omega_1-\omega_2)\approx\frac{e^3}{\hbar^2\varepsilon_0}\frac{z_{12}z_{23}z_{31}}{(\omega_3-\omega_{23}+i\Gamma_{23})}\left(\frac{N_1-N_3}{(\omega_1-\omega_{13}+i\Gamma_{31})}+\frac{N_1-N_2}{(-\omega_2+\omega_{12}+i\Gamma_{21})}\right) \quad (2)$$

where N_i are the population densities in the electron states i = 1,2, and 3, see Fig. 1, ez_{ij}, ω_{ij} and Γ_{ij} are the dipole matrix element, frequency, and broadening of the transition between states i and j. Assuming $N_2 \approx N_3$ for simplicity, both population differences in Eq. (2) are equal to the population inversion density ΔN_e which can be determined from a "gain=loss" condition. A $|\chi^{(2)}|\approx 4\times10^4$ pm/V was estimated for the DFG process in the devices.

Waveguide design and fabrication

The waveguide was designed for phase-matching, $k_3=k_1-k_2$, through controlling the waveguide cladding layers doping and thickness as well as the doping of the substrate. Using the effective refractive indices calculated for the TM_{00} modes of mid-infrared pumps and a THz wave, as well as the THz mode losses, the coherence length (see Eq. 1) was estimated to be approximately 50-80 μm in 25 to 60-μm-wide ridges.. The limiting factor for l_{coh} is the THz waveguide losses, which are calculated to be $\alpha\approx250$ cm^{-1}. The material was processed into deep etched ridge waveguides 2 mm long and 25 μm wide, tapered to 60 μm towards the front facet, with a 400-nm-thick Si_3N_4 insulating layer on the lateral walls of the ridge and a Ti/Au (20nm/400nm) top contact (Fig. 2a,b). A non-alloyed Ge/Au contact was deposited on the back. A high-reflectivity coating, consisting of Al_2O_3/Au (200nm/50nm) layers was evaporated on the back facet of the devices. Tapering was introduced in order to improve the outcoupling efficiency of THz radiation from the waveguide. The calculated waveguide modes for mid-IR and THz waves, along with the waveguide refractive index profile, are shown in Fig. 2c

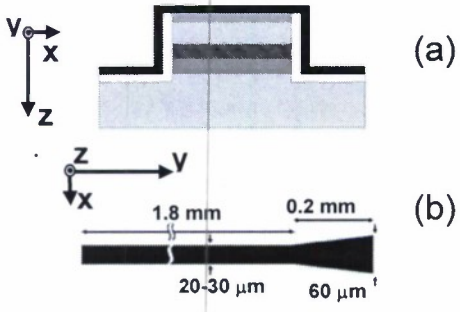

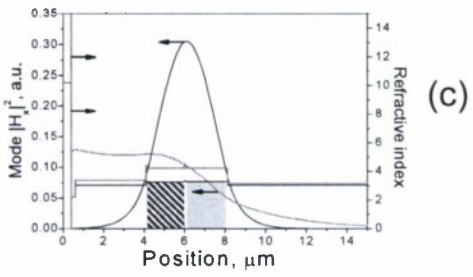

Fig. 2. (a) Waveguide structure: the gold layer is shown in black, the insulating Si_3N_4 layer is in white, and the semiconductor is in grey (for low-doped InP layers) and dark grey (for a high-doped InP layer and the two active region sections). The bound-to-continuum section is shaded. (b) Ridge waveguide shape, viewed from top: the back facet (left side) has a high-reflection coating. (c) The magnetic field intensity in the TM00 waveguide mode (right axis) and the refractive index profile (left axis) for λ=8.9 μm (thin black line) and λ=60 μm (thick grey line). Also shown in grey are the two sections of the active region.

Experimental Results

For measurements, devices were operated in pulsed mode with 60 ns pulses at a 250 kHz repetition rate. Radiation was collected using two 2"-diameter parabolic mirrors: one with a 5 cm focal length to collect light from the device and the other with a 15 cm focal length to refocus it onto a thermopile or mercury-cadmium-telluride (MCT) detector for mid-IR measurements or a He-cooled calibrated silicon bolometer for THz measurements. Mid-IR powers were corrected for the 70% collection efficiency of our setup. Spectra were taken with a Fourier transform infrared spectrometer. For THz measurements, mid-IR radiation was blocked using optical filters.

Because of subwavelength THz mode confinement in the waveguide, see Fig. 2(c), the THz DFG output from our devices is expected to be strongly divergent and THz outcoupling efficiency may be poor. A silicon hyper-hemispherical lens, attached to the device facet, may help to resolve these problems. Selected devices were equipped with a 2mm-diameter, 1.19mm-height high-resistivity silicon hyper-hemispherical lens. The lens was positioned to within 5μm of a device facet. For lens alignment, we imaged the mid-IR output from our devices with a MCT detector. Devices with a lens demonstrated a 25-fold increase in collected THz DFG power output, compared to devices without a lens. The increase stems from improved collection efficiency (from below 10% to approximately 50%) and improvements in THz out-coupling efficiency. Typical THz DFG spectra of a device with a lens, collected at different temperatures, are shown in Fig. 3(c).

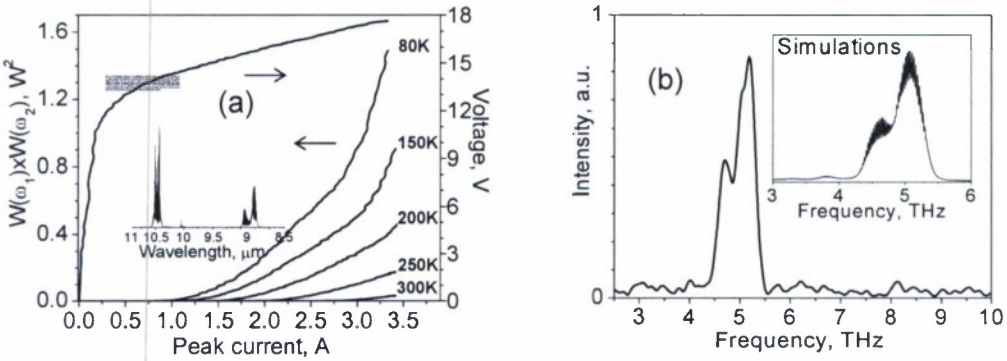

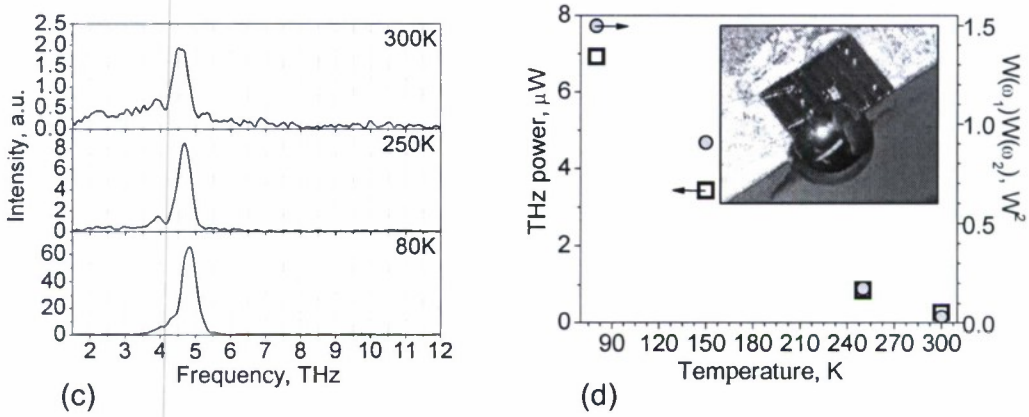

Fig. 3. (a) Product of mid-IR pump intensities versus current (left axis) and current-voltage (right axis) characteristics of a representative device. Inset: mid-IR emission spectrum of the device at 80K. (b) THz emission spectrum of the device in (a), measured at 80K. Insert: THz DFG spectrum, simulated from mid-IR spectrum in (a). (c) THz emission spectra of a device with a Si hyperhemispherical lens attached to the facet, at different temperatures. (d) Temperature dependence of the measured THz DFG signal intensity (right axis) and the product of mid-IR pump powers for a device with a Si lens. Inset: photograph of a device with a Si lens attached to a facet. The measurements in (d) and all the spectral measurements were done with a device operated with 3.5A current pulses.

THz output was observed up to RT, with THz power, corrected for the estimated 50% collection efficiency, decreasing from approximately 7μW at 80K to approximately 300nW at RT. This trend is demonstrated in Fig. 3(d), where we also plotted a product of mid-IR pump powers at different temperatures. The data in Fig. 3(d) indicate that the drop in THz power output originates mostly from a decrease of mid-IR pump powers, see Eq. (1), while THz DFG conversion efficiency remains constant, ~5 $\mu W/W^2$. Since mid-IR QCLs with CW power output levels of 1.5W at RT have already been demonstrated, it appears that a THz QCL source with microwatt-level CW THz output at RT is within reach. We believe that further device optimization, including the implementation of distributed feedback gratings to enforce single-mode emission for the two mid-IR pumps and the utilization of the surface-emission scheme for the THz radiation extraction, may lead to narrow-band THz DFG QCLs providing up to a milliwatt of the THz output power at RT

4. Record high temperature operation of Quantum Cascade Lasers

Prior to this work the highest operating temperature of THz QCLs was 169 K.

Further improvements in the maximum operating temperatures of THz QCLs can be achieved by improving both the active region and waveguide designs. In THz QCLs with metal-metal waveguides, 30-70% of the waveguide losses may originate from the losses associated with the metal claddings, the precise value depending on the emission wavelength, the active region design, and doping. The optical losses of the metal cladding can vary depending on the type of metal used.

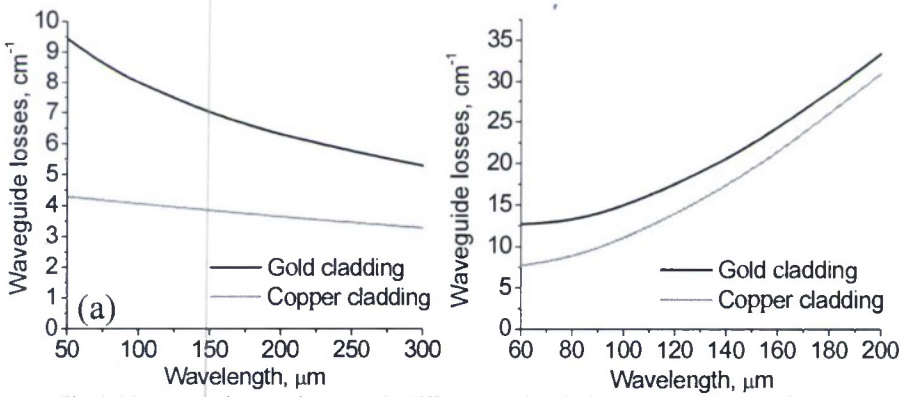

Fig. 4. (a) Calculated waveguide losses for different wavelengths in a metal-metal waveguide assuming a "lossless" active region. (b) Calculated waveguide losses in a metal-metal waveguide assuming a realistic active region design with an average doping of $5x10^{15}$ cm^{-3}. We note that long-wavelength, λ>200 μm, QCLs typically use lower doped active regions.

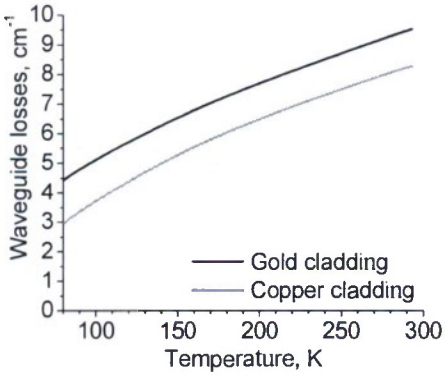

Fig. 5. Calculated temperature dependence of waveguide losses for 100 μm wavelength in a metal-metal waveguide assuming a "lossless" active region. Optical constants of metals were estimated using Eq. (1). The data for temperatures below 80 K is very sensitive to the purity of metals and is not shown.

Fig 4 compares calculated waveguide losses for 10μm-thick and infinitely wide MM THz QCL waveguides with claddings made of gold and copper for doping concentrations typical of QCL THz lasers.

In Fig. 5, the temperature dependence of the optical losses at 3 THz for 10μm-thick and infinitely wide MM waveguides with claddings made of gold and copper are plotted. The data indicate that

MM waveguides with copper claddings have smaller optical losses than MM waveguides with gold claddings even at cryogenic temperatures.
The data in Figs 4 and 5 demonstrate that, by using copper instead of gold, the waveguide losses in MM THz QCL waveguides can be significantly reduced.

Device structure, fabrication, and experimental results

To demonstrate the effect of the waveguide cladding material on the temperature performance of MM THz QCLs, we compared the performance of two sets of devices processed from the same active region material, but with two different MM waveguide cladding metals: gold and copper. The active region in our lasers was based on the conventional three-well resonant-phonon design. The QCL material was grown by MBE on an undoped GaAs substrate; the growth sequence started with a 250nm-thick undoped GaAs buffer layer, and was followed by a 300nm-thick $Al_{0.5}Ga_{0.5}As$ etch-stop layer, a 75nm-thick layer of GaAs n-doped to $5x10^{18}$ cm^{-3}, 226 stages of a active region design, but with a doping sheet density of $n_s=2.75x10^{10}$ cm^{-2}, and finally a 50nm-thick GaAs layer n-doped to $5x10^{18}$ cm^{-3}.

Devices were tested in pulsed mode with 30 ns pulses at a 1 kHz repetition rate. Peak powers were measured with a calibrated helium-cooled bolometer. Figure 6(a) displays the current density-voltage (I-V) characteristic of a representative device with gold cladding layers, as well as a typical emission spectrum. Devices processed into MM waveguides with a gold cladding typically operated up to 160-164 K. The light output as a function of current density (L-I) for the best performing device with gold MM waveguides, which operated up to 168 K, is shown in Fig. 6(b).

Devices processed into MM waveguides with copper cladding typically operated up to 170-174 K. The L-I characteristics for the best-performing device with copper cladding, which operated up to 178 K, are shown in Fig. 7(a), with the dependence of threshold current density on temperature being shown in Fig. 7(b). At high temperatures, the threshold current density displays an asymptotic dependence of $\sim exp\ (T/T_0)$ with $T_0 \approx 100$ K. We observed a similar asymptotic dependence with similar T_0 for devices processed into MM waveguides with gold cladding. We attribute the observed improvement in temperature performance in copper MM waveguide devices to the superior optical properties of copper over those of gold

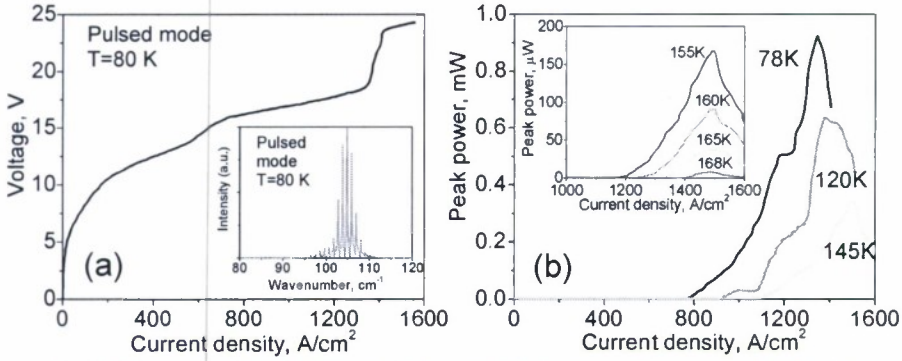

Fig. 6. (a) Current density-voltage characteristic and an emission spectrum (inset) of a representative device processed with a gold metal-metal waveguide. Devices processed with a copper metal-metal waveguides displayed similar current density-voltage characteristics and emission spectra. (b) Light intensity-current density (LI) characteristics of the best-performing device with a gold metal-metal waveguide, 1.3mm-long and 150μm-wide. Inset: the LI characteristics of the device close to the maximum operating temperature of 168 K. The data are not corrected for an estimated 10% power collection efficiency.

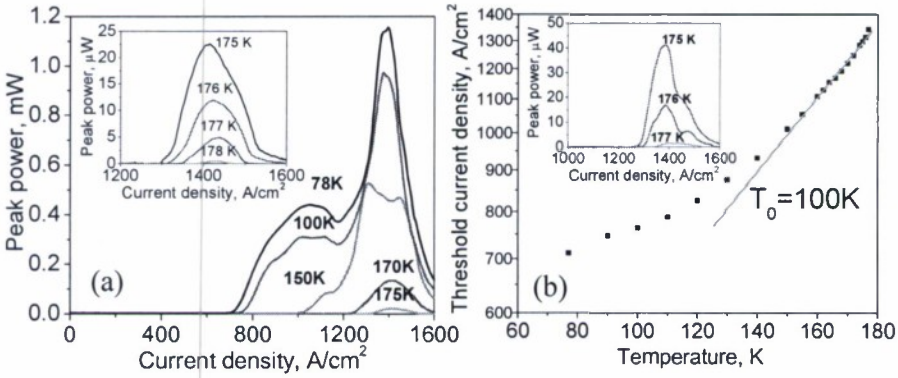

Fig. 7. (a) The LI characteristics of a 1.4mm-long and 125μm-wide device with a copper metal-metal waveguide. Inset: the LI characteristics of the device close to the maximum operating temperature of 178 K. The data are not corrected for an estimated 10% power collection efficiency. Dips in the LI characteristics at current density ~1150 A/cm^2 are due to some of the laser emission lines coincide with atmospheric absorption lines. (b) Threshold current density as a function of temperature for the device in (a). Inset: the LI characteristics of another device with a copper metal-metal waveguide, 1.6mm-long and 100μm-wide, close to its maximum operating temperature of 177 K.

5. Surface-emitting THz QCL with double-metal waveguide: up to 10mW of collected THz power

The solution to the problem of significant trapping of power in THz QC lasers is a second-order grating for surface emission. The grating provides better out-coupling efficiency for THz and less beam divergence than edge-emitting QCL. Earlier in this AFOSR contract surface-emitting THz QCL with double-metal waveguide that provided up to 50μW of low-divergence

radiation output at 3THz were demonstrated. The structure was implemented in a dual metal surface plasmon waveguide, since the latter has been shown to give the highest operating temperature in edge emitting THz QC lasers. The power of the surface-emitting THz QC lasers was improved since then by more than 100 times, by using a better QCL active region and the waveguide design. The QCL material was supplied by Prof. Edmund Linfield, University of Leeds, UK, a leader in THz QC laser growth who demonstrated with the group of Tredicucci the first THz QC laser. Edge emitting devices were processed into 150μ-wide double-metal waveguides.

Experimentally a considerable improvement in temperature performance and the output power with the new generation of devices was observed . In particular, the maximum THz output power has been improved from 50μW to almost 10mW and the maximum operating temperature has been improved from 63K to 70K. The measurement results are summarized in Fig. 8.

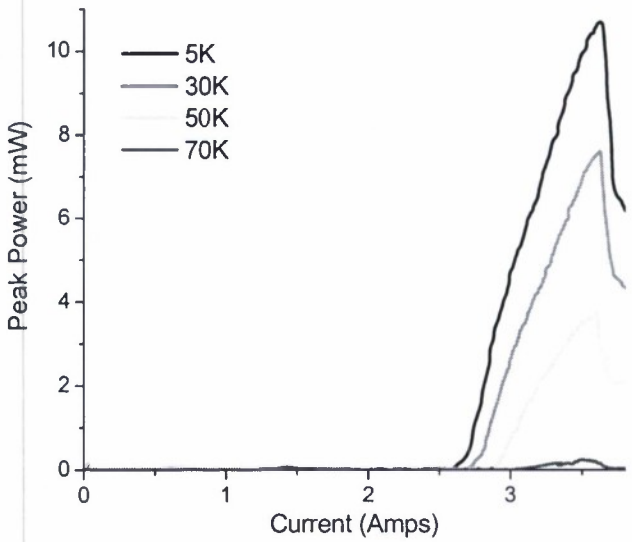

Fig. 8. L-I characteristics at different temperatures of λ= 100μm (3 THz) surface emitting QC laser with the improved second-order grating and active region design.

Fig. 9 shows the spectra of the improved surface emitting DFB THz QCLs of different grating periodicities. Note the single mode operation with a factor of 10^3 side mode suppression ratio.

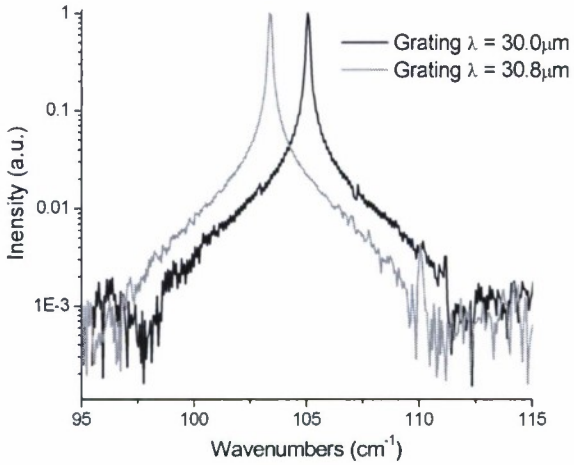

Fig. 9. Single mode spectral characteristics of ~3THz Surface emitting DFB QCLs with different grating periodicities.

Finally, Fig 10 shows the far field profile of the device.

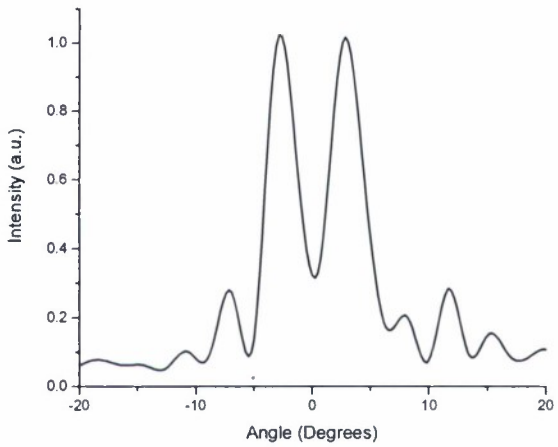

Fig. 10 THz QCL far field profile indicating a beam divergence of 8 deg (FWHM). Note that two-lobe profile can be reduced to a one-lobe profile, by incorporating a π-shift in the middle of the grating [G. Witjaksono and D. Botez, APL **78,** 4088 (2001)].

The divergence is reduced to a few degrees compared to edge emitting THz QC lasers at the same wavelength, for which the beam divergence approaches π due to sub-wavelength nature of the device aperture normal to the layers. This high directionality will open up opportunities for THz surface emitting QC lasers.

6. Publications:

1. M. A. Belkin, F. Capasso, F. Xie, A. Belyanin, M. Fischer, A. Wittmann, J. Faist, "Room temperature terahertz quantum cascade laser source based on intracavity difference-frequency generation"
   Applied Physics Letters **92**, 201101 (2008)

2. M. A. Belkin, J. A. Fan, S. Hormoz, F. Capasso, S. P. Khanna, M. Lachab, A. G. Davies, E. H. Linfield, "Terahertz quantum cascade lasers with copper metal-metal waveguides operating up to 178 K"
   Optics Express **16**, 3242 (2008)

3. J. A. Fan, M. A. Belkin, F. Capasso, S. P. Khanna, M. Lachab, A. G. Davies, and E. H. Linfield "Wide-ridge metal-metal terahertz quantum cascade lasers with high-order lateral mode suppression"
   Applied Physics Letters **92**, 31106 (2008)

4. M.A. Belkin, F. Capasso, A. Belyanin, D.L. Sivco, A.Y. Cho, D.C. Oakley, C.J. Vineis, G.W. Turner, "Terahertz quantum-cascade-laser source based on intracavity difference-frequency generation," *Nature Photonics* **1**, 288 (2007).

5. J.A. Fan, M.A. Belkin, F. Capasso, S. Khanna, M. Lachab, A.G. Davies, E.H. Linfield, "Surface emitting terahertz quantum cascade lasers with a double-metal waveguide," *Opt. Express* **14**, 11672 (2006).

6. M. A. Belkin, M. Troccoli, L. Diehl, F. Capasso, A. Belyanin, D. L. Sivco and A. Y. Cho "Quasiphase matching of second-harmonic generation in quantum cascade lasers by Stark shift of electronic resonances"
   Applied Physics Letters **88**, 201108 (2006)

9. Inventions or patent disclosures:

One patent has been filed in 2007:
M.A. Belkin, F. Capasso, A. Belyanin, "Terahertz quantum cascade laser source based on intra-cavity difference-frequency generation."